

Please cite the Published Version

Doyle, Aidan  and Hajimirzaee, Saeed (2020) 3D printed catalytic converters with enhanced activity for low-temperature methane oxidation in dual-fuel engines. *Fuel*, 274. p. 117848. ISSN 0016-2361

DOI: <https://doi.org/10.1016/j.fuel.2020.117848>

Publisher: Elsevier

Version: Accepted Version

Downloaded from: <https://e-space.mmu.ac.uk/625544/>

Usage rights:  Creative Commons: Attribution-Noncommercial-No Derivative Works 4.0

Additional Information: This is an Author Accepted Manuscript of a paper accepted for publication in *Fuel*, published by and copyright Elsevier.

Enquiries:

If you have questions about this document, contact openresearch@mmu.ac.uk. Please include the URL of the record in e-space. If you believe that your, or a third party's rights have been compromised through this document please see our Take Down policy (available from <https://www.mmu.ac.uk/library/using-the-library/policies-and-guidelines>)

3D printed catalytic converters with enhanced activity for low-temperature methane oxidation in dual-fuel engines

Saeed Hajimirzaee, Aidan M. Doyle*

Department of Natural Sciences, Manchester Metropolitan University, Chester Street, Manchester M1 5GD, United Kingdom;

* corresponding author a.m.doyle@mmu.ac.uk

Abstract

Catalytic converters with non-linear channel structures were prepared using 3D printing and tested in the oxidation of methane in a simulated dual-fuel engine exhaust stream. The design used a simple repeating angular offset between adjacent layers, which was sufficient to introduce complexity with minimal software programming. All 3D printed substrates were mechanically stable and, following washcoating with a composite catalyst, demonstrated higher catalytic activity in methane oxidation than a commercial honeycomb substrate. The methane conversion at e.g. 510 °C was 12.6% on the commercial sample, 72.6% for 90 °, 80.1% for both 30 ° and 45 °, and 89.6 % for the 60 ° oriented structures. This enhancement is attributed to the increased turbulence/mass transfer and surface area than are possible using conventional straight-channelled substrates. Computational fluid dynamics (CFD) analysis confirmed that the higher methane conversion over 3D printed substrates is due (at least partially) to its higher turbulence kinetic energy. Backpressures over the 3D printed structures were also experimentally measured and compared with the conventional honeycomb monolith.

Keywords: dual fuel, methane oxidation, 3D print, additive manufacturing, ceramic, CFD

1. Introduction

Diesel engines are preferred for heavy-duty applications such as domestic and commercial transportation due to their durability, fuel efficiency and higher power density. However, these engines greatly contribute to environmental pollution caused by harmful exhaust emissions[1]. The main pollutants from diesel engines are CO, CO₂, unburnt hydrocarbon, NO_x and particulate matter (PM) which have an adverse effect on the natural

29 environment, land, water, air and, therefore, human health[2]. In 2012, the emissions from diesel engine exhaust
30 were classified as carcinogenic to humans by the International Agency for Research on Cancer (IARC), which
31 is part of the World Health Organization (WHO)[3]. Stricter new regulations on exhaust emission and depletion
32 of fossil fuel resources have forced companies to utilise an alternative fuel and/or technology to overcome this
33 problem. Supplementary fuels such as LNG[4], LPG[5], CNG[6], biogas[7], methanol[8], hydrogen[9], and
34 ammonia[10] have been studied in dual fuel diesel engines, in which LNG and CNG have attracted the greatest
35 attention due to their cost-effectiveness and environmental benefits[11]. Natural gas, which contains mostly
36 methane, is a promising alternative fuel for the transportation sector because it is available at a lower price and
37 produces lower carbon emissions. It has the lowest carbon to hydrogen ratio of any hydrocarbon and, therefore,
38 produces less CO₂ and nearly zero smoke or PM, which is almost impossible in diesel-only engines. Moreover,
39 it significantly reduces the NO_x emission by approximately 50–80%[12]. Other advantages of natural gas
40 include its higher octane number, which means the gas burns hotter and, therefore, can reduce the knocking
41 effect, especially in diesel engines where the compression ratio is relatively high[13]. Furthermore, it has better
42 mixing with air, causing uniform temperature distribution and higher thermal efficiency, which can only be
43 achieved on diesel engines at high loads[14]. However, one of the main drawbacks of using natural gas in dual
44 fuel engines is higher emission of carbon monoxide and unburnt methane from the engine known as “methane
45 slip”. This phenomenon is more dominant at low to medium loads. It has been reported that around 90% of the
46 total hydrocarbons (THC) emissions in a CNG/diesel dual fuel engines are unburned methane[6]. The amount
47 of methane emission on a marine vessel with a LNG/diesel dual fuel engines was reported to be around 7 g.kg⁻¹
48 ¹ LNG at high load, rising to 23-36 g.kg⁻¹ LNG at lower loads.

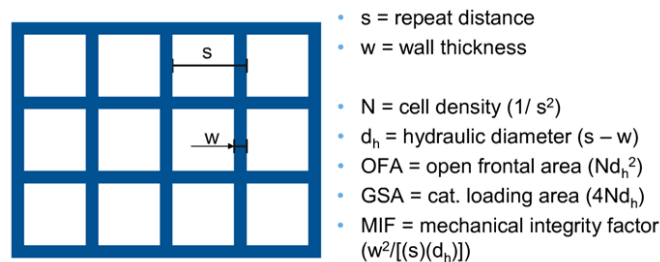
49 One practical solution to effectively reduce emission content in the exhaust is to use a catalytic converter.
50 Catalytic converters are made of ceramic or metal substrates coated with active catalysts which are widely used
51 in environmental applications such as three-way catalyst (TWC) for CO and hydrocarbon oxidation and
52 selective reduction of NO_x in small engines; elimination of volatile organic compounds (VOCs) and other
53 organic compounds; hazardous air pollutants (HAPs); and odorous emissions from gaseous effluents[15].

54 In the auto industry, the common catalyst support for exhaust gas treatment has a monolithic honeycomb
55 structure with a series of parallel tubes and cell density ranging from 300 to 1200 CPSI (cells per square inch).
56 The main reasons that the monolithic honeycomb support is still the first choice for catalyst support in the
57 exhaust after-treatment systems are: available and cost-effective extrusion technology; straightforward

58 washcoating methods; flexibility in cell design; low-pressure drop; and good heat and mass transfer rates [16].
59 Generally, an ideal monolith with high efficiency should have the following criteria: 1) high surface area to
60 volume ratio; 2) high penetrability with low back pressure; 3) high mechanical strength; 4) low thermal
61 expansion; 4) high-temperature shock resistance; 5) corrosion resistance; 6) chemical inertness[17]. However,
62 having all these properties in one package is extremely challenging, and even the best commercial products
63 cannot meet all these criteria.

64 Ceramics are the most frequently used materials for manufacturing monolith. Different ceramic materials such
65 as aluminium titanate (Al_2TiO_5), calcium titanate (CaTiO_3) and silicon carbide (SiC) have been used[18], yet
66 cordierite, with the chemical composition of $2\text{MgO} \cdot 2\text{Al}_2\text{O}_3 \cdot 5\text{SiO}_2$, has become the material of choice owing to
67 its relatively low thermal expansion coefficient and high thermal shock resistance[19].

68 The channel size and structure of the substrate play an important role in the overall performance. The channels
69 of the most common substrates typically have square, circular or triangular shaped cross-sections that extend in
70 one dimension, similar to a honeycomb structure. These channels provide space for the flow of gases and/or
71 liquids that interact with the active catalyst dispersed on the channel walls via washcoating.[20] Figure 1 shows
72 the relation between wall thickness (w), repeat distance (s), and cell density (N) which is defined as channels
73 per unit of cross-sectional area in inches (CPSI). Other parameters such as open frontal area (OFA) and catalyst
74 loading areas (GSA) can be calculated from w and s .



75
76 Figure 1. Relation between monolith structural parameters.

77
78 Ceramic substrates with CPSI in the range 25-1200 have been manufactured but the most common range for
79 automotive catalytic converter applications is 400-900 CPSI and 0.004 in (0.1 mm) wall thickness[17]. Ultra-
80 thin wall (UTW) ceramic substrates with 900-1200 CPSI and 0.002 in (0.05 mm) wall thickness have been also
81 manufactured and tested. It has been shown that the UTW substrates provide the possibility of reducing the
82 costs of the exhaust system by reducing the amount of precious metals and/or reducing the catalyst volume.

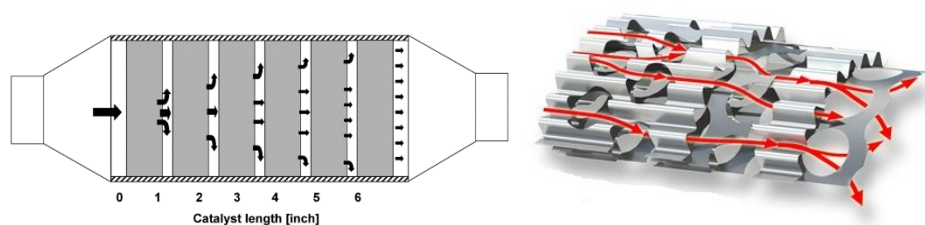
83 However, these substrates have lower mechanical strength and shorter lifespan due to being more prone to
84 damage[21].

85 Metallic monolith structures have been manufactured as catalytic converter supports. These substrates can be
86 made with thinner walls and bigger open frontal areas close to 90%, allowing a lower pressure drop. The material
87 used in metallic substrates are commonly ferritic stainless steel alloy with chrome, aluminium and rare earth
88 metals. Typical CPSI values for these metallic monoliths lie in the range 400-600 CPSI with 0.002 in wall
89 thickness[16]. Another advantage of metallic monoliths is their high thermal conductivity and low heat capacity,
90 which allow faster heating during the engine start-up thereby minimising the light-off time[22]. It is also
91 possible to construct the channels with corrugated foils to induce turbulent flow and increase the mass transfer
92 and therefore catalyst efficiency[23]. One of the main disadvantages of metallic monoliths is their higher
93 manufacturing cost. The thermal expansion coefficient is much greater for metallic substrates which means they
94 require special bonding techniques to adhere washcoat onto the metal surface[24].

95 Another technology that has been developed to improve the efficiency of catalytic converters employs a
96 periodical reversal of gas flow through the catalyst. This technology traps the heat energy from inside the
97 monolith to increase the catalyst operating temperature. This has been used in the purification of industrial off-
98 gases containing VOCs[25]; oxidation of methane and CO emitted from dual LNG dual-fuel diesel engines[26,
99 27]; NO_x reduction from diesel engines; and emission control during cold start of automotive engines[28]. The
100 main drawback is that the performance of the system strongly depends on the temperature of the exhaust and
101 catalytic reactor. It has been reported that the technology fails to operate efficiently if the reactor temperature
102 or concentrations of HC and CO are too low[27].

103 Introducing turbulent flow is a promising approach to increase catalytic converter efficiency and/or facilitate a
104 more uniform temperature profile across the catalytic converter[29, 30]. In a conventional extruded monolith,
105 the flow in the frontal section is a jet flow; however it is fully laminar inside the narrow channels,. It is well
106 known that in laminar flow the catalytic reaction is diffusion limited; therefore, different methods have been
107 proposed to increase turbulence in the inlet flow (not inside the channels). One method is to add a device before
108 the monolith to induce turbulence to the gas, prior to entering the channels. Agrawal et al.[31], showed that the
109 turbulence device with a swirl blade configuration is effective in improving the conversion efficiency of the
110 catalytic converter, with lower backpressure relative to other configurations.

111 Another approach is to create the turbulent flow inside the channels. Figure 2 shows two structures which was
112 proposed by Brük et al. [32], longitudinal structure (LS) and perforated structure (PS). In the LS structure, the
113 monolith is divided into disks that lie perpendicular to the direction of gas flow to generate turbulence on the
114 frontal section of the monolith. Despite having an efficient catalytic converter, the method was not efficient for
115 mass production, due to the high production cost and complicated canning process. In the PS structure, the
116 authors employed corrugated and flat metallic foils containing 8 mm diameters holes to facilitate radial flow
117 inside the channels, which increased conversion and lowered backpressure. However, the differences in thermal
118 expansions between metallic substrates and washcoat have minimised the usage of metal based catalytic
119 converters in original equipment manufacturer (OEM) diesel engines, which makes ceramics the most
120 promising material for such applications.



121 Figure 2 Longitudinal Structure (left) and Perforated Structure (right) for enhanced mass flow in catalytic converter.[32, 33]
122 3D printing has attracted more attention in recent years as a versatile and low-cost technology for rapid
123 casting/prototyping of a variety of materials, including ceramics.[34, 35] Thanks to its almost unlimited axial
124 flexibility, this technique enables rapid production of customised shapes, the design of which can vary through
125 each of all three spatial dimensions. In the case of catalytic converter substrates, the versatility offered by 3D
126 printing greatly increases the range and complexity of channel structures that are not available using
127 conventional extrusion methods. A number of 3D printing techniques are suitable for ceramics, the choice of
128 which is determined by whether the ceramic material is the form of slurry, powder, bulk solid or paste. Examples
129 of available technologies for 3D printing of ceramics are liquid deposition modelling (LDM); laminated object
130 manufacturing (LOM); for bulk solid/paste materials, stereolithography (SLA); digital light processing (DLP);
131 two-photon polymerisation (TPP); ink-jet printing (IJP); direct ink writing (DIW) and three-dimensional
132 printing (3DP) for slurry based materials; selective laser sintering (SLS); and selective laser melting (SLM) for
133 ceramic powder[36]. Here we report the design and printing of substrate structures with greater complexity than
134 those available in conventional honeycomb arrangements with straight channels and evaluate their performance
135 in the catalytic oxidation of methane.

136

137 2. Experimental method

138 2.1 Substrate 3D printing

139 Small samples (Ø2.0 cm x H2.0 cm) were printed using cordierite precursors on a WASP 4070 ceramic 3D
140 printer with nozzle diameter 0.7 mm. The technique for deposition of material is LDM (similar to robocasting),
141 which consists of depositing layers of ceramic material (cordierite paste) until the model is formed. Cordierite
142 was synthesised according to a solid-state reaction of cordierite precursors based on a composition available in
143 literature[37, 38]. A paste was prepared by dry mixing of cordierite precursors in powder form according to
144 Table 1, followed by adding water and ethylene glycol (20% of solid weight) with ratio 6:1. The mixture was
145 kneaded until a uniform paste was formed. The paste was then used to print the substrates.

146

Table 1 Composition of cordierite precursor for solid mixing.

Compound	Talc	Kaolin	Al ₂ O ₃	B ₂ O ₃	Cordierite
Weight (%)	35.4	46.7	12.9	1.7	3.3

147

148 Printed samples were dried at room temperature for 24 hours, heated at 1 °C.min⁻¹ ramp rate and sintered at
149 1200 °C to form the cordierite phase. Subsequently, the substrates were washcoated according to the method
150 described in section 2.2. The weight of washcoat on the substrates was adjusted to be around 0.1 g.

151

152 2.2 Catalyst preparation

153 The catalyst washcoat was chosen to be applicable to auto emission control. The catalyst contained Pd:Pt with
154 1:1 ratio doped on Al₂O₃/HY zeolite and promoted by cerium, zirconium and titanium oxide. The zeolite used
155 in this formulation was prepared using a geothermal silica source which we previously found to be active in
156 methane oxidation[39]. This activity is attributed to the presence of sodium ions in the structure of the
157 zeolite[40].

158 The washcoat catalyst was prepared according to the following procedure:

- 159 - Support suspension: 1000 mg of support powder was prepared by mixing HY Zeolite, γ -Al₂O₃ (Sigma-
160 Aldrich, activated, neutral), TiO₂ (Millennium PC500), CeO₂ (Sigma-Aldrich, nanopowder <25nm particle

161 size), and ZrO₂ (Sigma-Aldrich, 5µm, 99%) with mass ratio 12:3:3:1:1, respectively. 100ml of water was
162 added to the solid powder and stirred, and the pH was adjusted to 11 by adding NH₄OH solution.

163 - Precious metal solution: 290 mg Pd(NO₃)₂.H₂O (Alfa Aesar, 99.8%) and 283 mg K₂PtCl₄ (Precious Metals
164 Online, 99 %), were dissolved in distilled water in two separate 50 ml volumetric flasks, followed by
165 ultrasonic treatment for 15 min. Precious metal solution was added dropwise to the support suspension,
166 stirred for 2 hours followed by ultrasonic treatment for 15 min. The resulting suspension was used as
167 washcoat for the substrate. The solid powder was extracted from the catalyst suspension by filtration and
168 converted to pellet form by compression, crushing and finally sieving.

169 - Both catalyst pellets and washcoated 3D printed substrates were dried at 50 °C for 24 hours and calcined at
170 550 °C for 8 hours.

171

172 **2.3 Catalyst characterisation**

173 X-ray diffraction (XRD) analysis of powder catalyst was performed at ambient conditions using a Panalytical
174 X'Pert Powder diffractometer with Cu K α radiation ($\lambda = 1.5406 \text{ \AA}$). The diffraction pattern was recorded in the
175 range 5 to 120° with a step size 0.013 and step time 200 s, using an X-ray tube operated at 45 kV and 40 mA
176 with fixed 4° programmable anti-scatter slit. Scanning electron microscopy (SEM) images were recorded using
177 a ZEISS Supra 40VP microscope. Prior to imaging, the samples were sputter-coated with a thin layer of gold.
178 Nitrogen adsorption/desorption measurement was carried out on a Micromeritics ASAP 2020 Surface Analyser
179 at 77 K. Samples were degassed under vacuum ($p < 10^{-5}$ mbar) for 3 hour at 300 °C prior to analysis. BET
180 surface areas were calculated in the relative pressure range 0.05-0.30.

181

182 **2.4 Catalyst testing**

183 To investigate the effect of structure on substrate performance, washcoated samples were tested under similar
184 conditions in methane oxidation. The feed contains 5 vol.% CH₄, 10 vol.% O₂, 85 vol.% He with GHSV of 400,
185 800 and 1200 h⁻¹. The weight of catalyst either in pellet form or on the substrate is 0.1 g. When in pellet form,
186 the catalyst was mixed with glass beads, which acted as a diluent to prevent formation of hotspot zones on the
187 catalyst by reducing its activity without affecting the fluid flow through the catalyst bed[41].

188

189 **2.5 CFD analysis**

190 The effect of structure on fluid dynamics, turbulence and backpressure was analysed using ANSYS Fluent v19.1.
 191 The fluid domain was meshed using a tetrahedron method with refined mesh near the walls (Figure 3).
 192 Realizable k-epsilon turbulence with default constants were used as a model. Air at room temperature and
 193 pressure was used as the fluid and cordierite as the solid material. Boundary conditions are as follow: inlet
 194 velocity 0.0066 m.s⁻¹ (corresponding to GHSV=1200 h⁻¹), k (turbulent kinetic energy) = 0.0015 m².s⁻², ϵ
 195 (turbulence dissipation rate)=0.00679 m².s⁻³ , outlet gauge pressure = 0 Pa, temperature = 20 °C. Equations to
 196 calculate k and ϵ are as follows[42]:

197
$$k = \frac{3}{2}(u_{avg}I)^2 \quad I = 0.16Re^{-\frac{1}{8}} \quad \epsilon = \frac{C_u^{\frac{3}{4}}k^{\frac{3}{2}}}{l} \quad l=0.07L$$

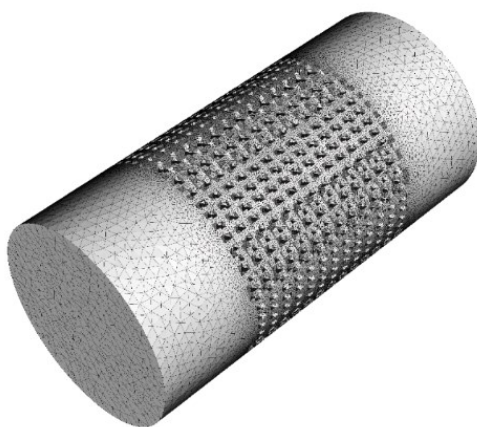
198 where C_u is an empirical constant specified in the turbulence model, which is approximately 0.09, and L is the
 199 diameter of the pipe. Number of nodes and elements are listed in Table 2.

200

201 Table 2 Number of nodes and elements for different structures

Structure	Number of Nodes	Number of Elements
30 °	1136074	5100584
45 °	1004929	4694231
60 °	1038631	4300399
90 °	1572989	2192526
CPSI 400	248694	1468540

202



203

204 Figure 3. Fluid domain mesh for CFD analysis.

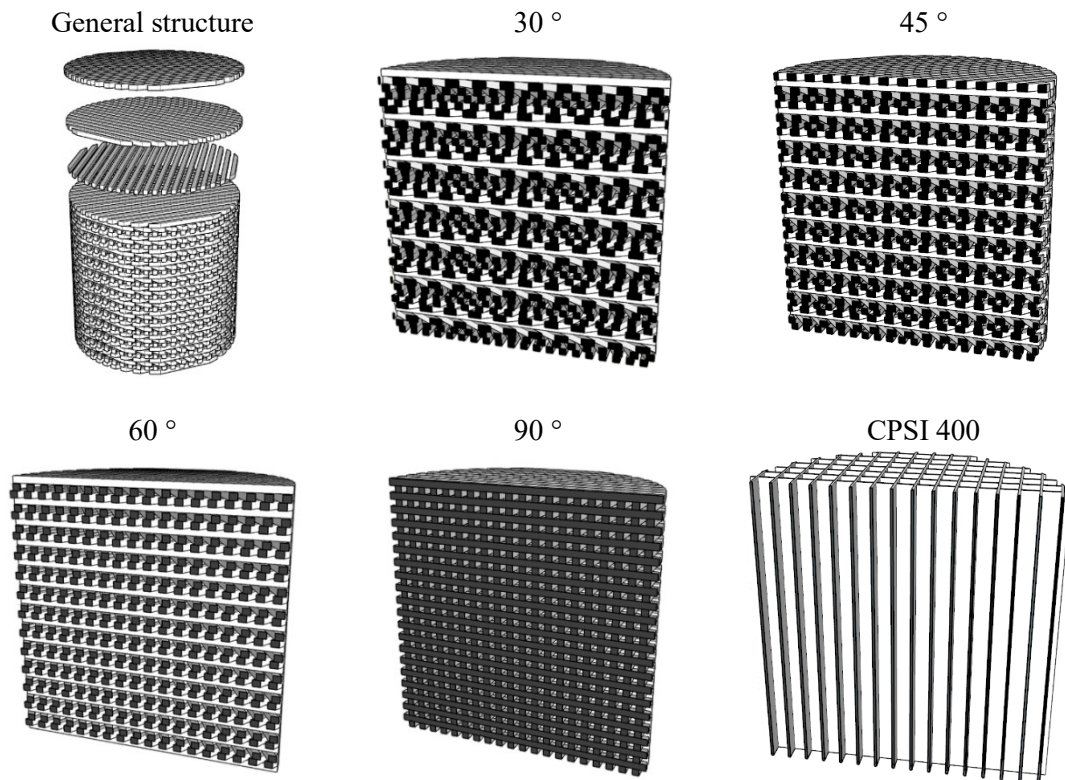
205

206

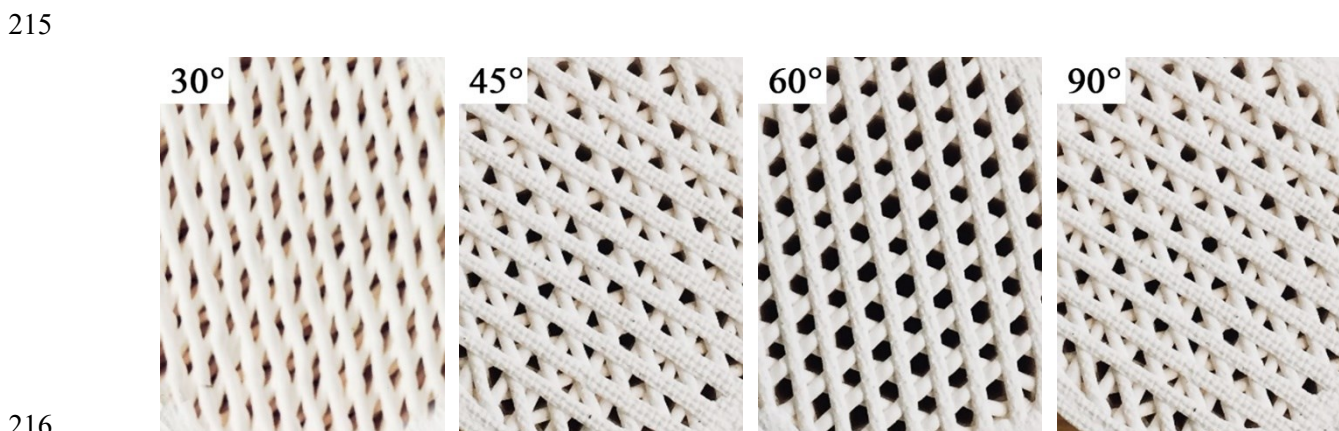
207 **3. Results and discussion**

208 **3.1 Ceramic 3D printing**

209 SketchUp was used as the 3D modelling software to design the different structures. The structure is made of
210 layers, which are printed at an offset angle to the preceding layer, and so on, vertically upwards (Figure 4). A
211 conventional honeycomb substrate with straight channels was also designed for comparison purposes. The CAD
212 (computer-aided design) were later used in slicing software to generate the g-code for 3D printing.



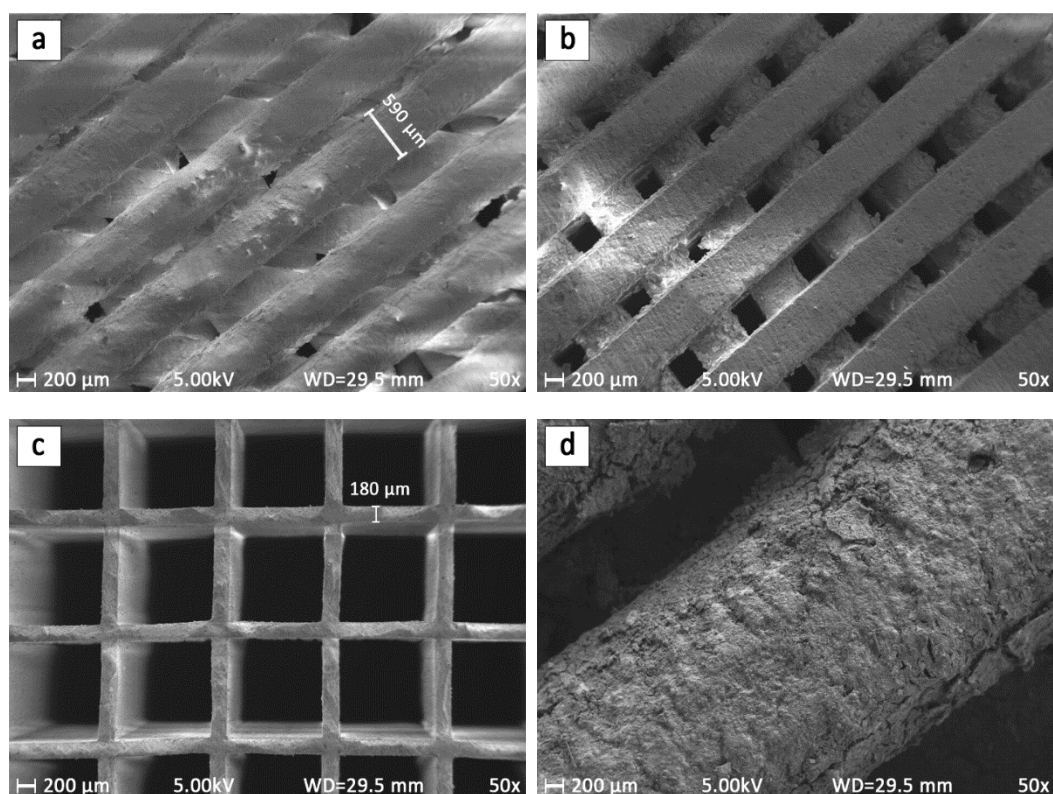
213
214 Figure 4. General structure and cross sectional view of 3D printed ceramic substrates.



216
217 Figure 5 3D printed substrates ($\varnothing 2.0$ cm x H2.0 cm) with different layer rotation offset (after sintering).

218

219 Figure 5 shows optical images of 3D printed substrates with different rotation angles after sintering (but before
220 washcoating). The SEM images of samples after washcoating are shown in Figure 6. Figure 6.a. shows SEM
221 image of substrate with 45 ° offset angle. These samples show less open area, after washcoat, compared to 90 °
222 (Figure 6.b.) or the commercial sample (Figure 6.c.). Figure 6.d. shows the washcoat in more detail. It should
223 be noted that the 3D printed monolith was prepared with relatively thick walls; this is due to limitations in
224 extrusion of material through the nozzle using the LDM method. From SEM images on Figure 6, this value is
225 around 0.59 mm, equivalent to CPSI 100. The wall thickness for the commercial substrate with CPSI 400 is
226 0.18 mm which is 70% less than the 3D printed sample.
227 Honeycomb monolith structures have been manufactured and tested by 3D printing of ceramic material
228 especially cordierite using robocasting or LDM methods[43-45]. Other 3D printing methods such as DLP has
229 shown promising results to manufacture structures with thinner walls and more details. However, material
230 properties (e.g. ceramic particle size and resin formulation) or printing parameters (e.g. layer thickness and
231 exposure time) need to be optimised for a successful print with desirable mechanical properties[46].



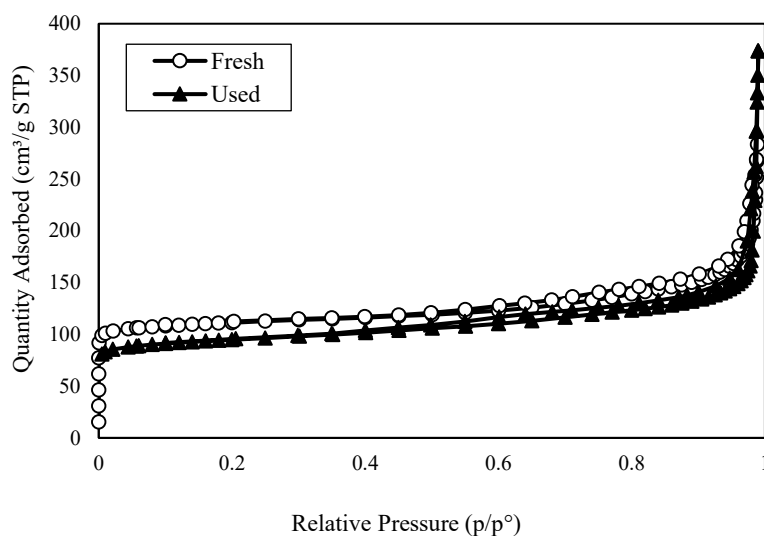
232
233
234 Figure 6 SEM imaging of 3D printed substrates; a) 45 °, b) 90 °, c) commercial, d) catalyst washcoat on substrate.
235

236 **3.2 Catalyst characterisation**

237 The properties of the fresh and used catalyst support powder, measured by nitrogen adsorption-desorption at 77
 238 K, are listed in Table 3. S_{BET} is the surface area calculated by BET method, V_t is the total pore volume calculated
 239 at $P/P^*=0.98$, V_{mes} is the volume of mesopores calculated using BJH method during desorption, V_{mic} is the
 240 volume of micro-pores calculated using t-plot method during desorption and d_{BJH} is the average diameter of
 241 mesopores calculated using BJH method during desorption. Figure 7 illustrates the adsorption-desorption
 242 isotherm of the catalyst washcoat before and after reaction. The graph is consistent with typical type IV
 243 adsorption isotherm with H3 hysteresis. Such isotherms are normally for aggregates of plate-like particles that
 244 form slit-like pores[47]. Overall, there were slight decreases in porosity characteristics, particularly so for V_{mic}
 245 which may have been caused by carbon deposition and/or metal nanoparticles sintering within the micropores.

246 Table 3 Physical properties of catalyst support powder measured by N₂ adsorption-desorption at 77 K.

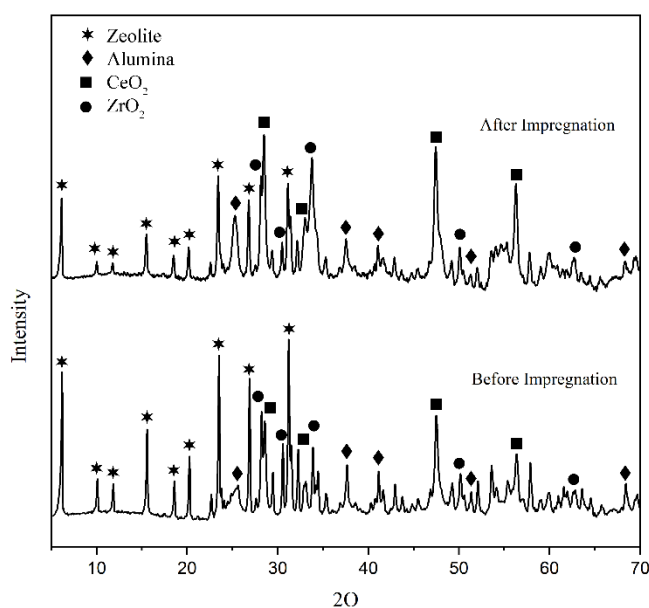
	$S_{BET}(\text{m}^2.\text{g}^{-1})$	$V_t(\text{m}^3.\text{g}^{-1})$	$V_{mes}(\text{m}^3.\text{g}^{-1})$	$V_{mic}(\text{m}^3.\text{g}^{-1})$	$d_{BJH}(\text{nm})$
Fresh	363	0.44	0.28	0.16	14.3
Used	311	0.36	0.27	0.09	13.7



248 Figure 7 N₂ adsorption/desorption isotherms of fresh and used (TOS = 90 h) catalyst support powder.

249 Figure 8 shows the the XRD pattern of catalyst washcoat before and after impregnation. The XRD confirms the
 250 characteristic crystallinity of Faujasite type zeolite, Al₂O₃, CeO₂ and ZrO₂; the TiO₂ peaks are not visible due
 251 to their relatively weak intensities, low concentration of TiO₂ in the overall sample and overlap with other
 252 reflections. There was a noticeable decrease in the peak intensities for zeolites. This is due to the partial
 253 structural decay of zeolites resulting from the metal impregnation and additional associated calcination step.
 254 Moreover, Pd or Pt peaks are not detected due to their low content and implied high dispersion. There was

256 practically no change observed in the d -spacing values of the zeolite, which proves that the zeolitic crystalline
257 structure was unchanged after impregnation. Figure 9 shows TEM images of fresh catalyst washcoat and after
258 90 hours consecutive stability testing. The stability tests were conducted using a reactant stream comparable to
259 an engine exhaust stream, including the presence of steam i.e. 450 °C, 5% CH₄, 20% O₂, 3% CO, 7% CO₂, 6%
260 H₂O, GHSV 1200 h⁻¹). Although slight sintering is observed for only very fine particles, the metal particles size
261 has not been changed significantly. This confirms the catalyst stability against sintering for an extended time.

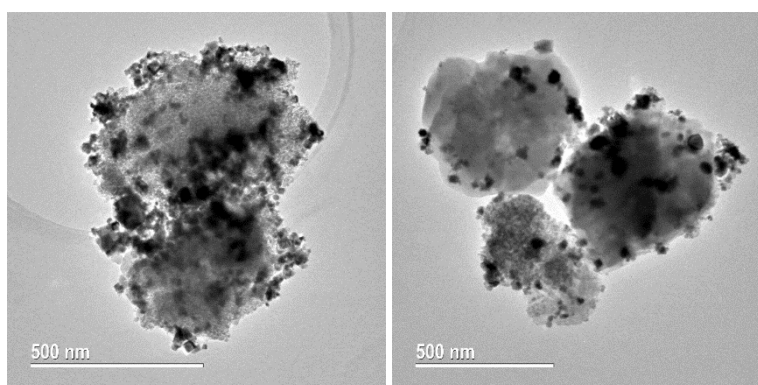


262

263

Figure 8 XRD pattern of catalyst support powder, before and after precious metals impregnation.

264



265

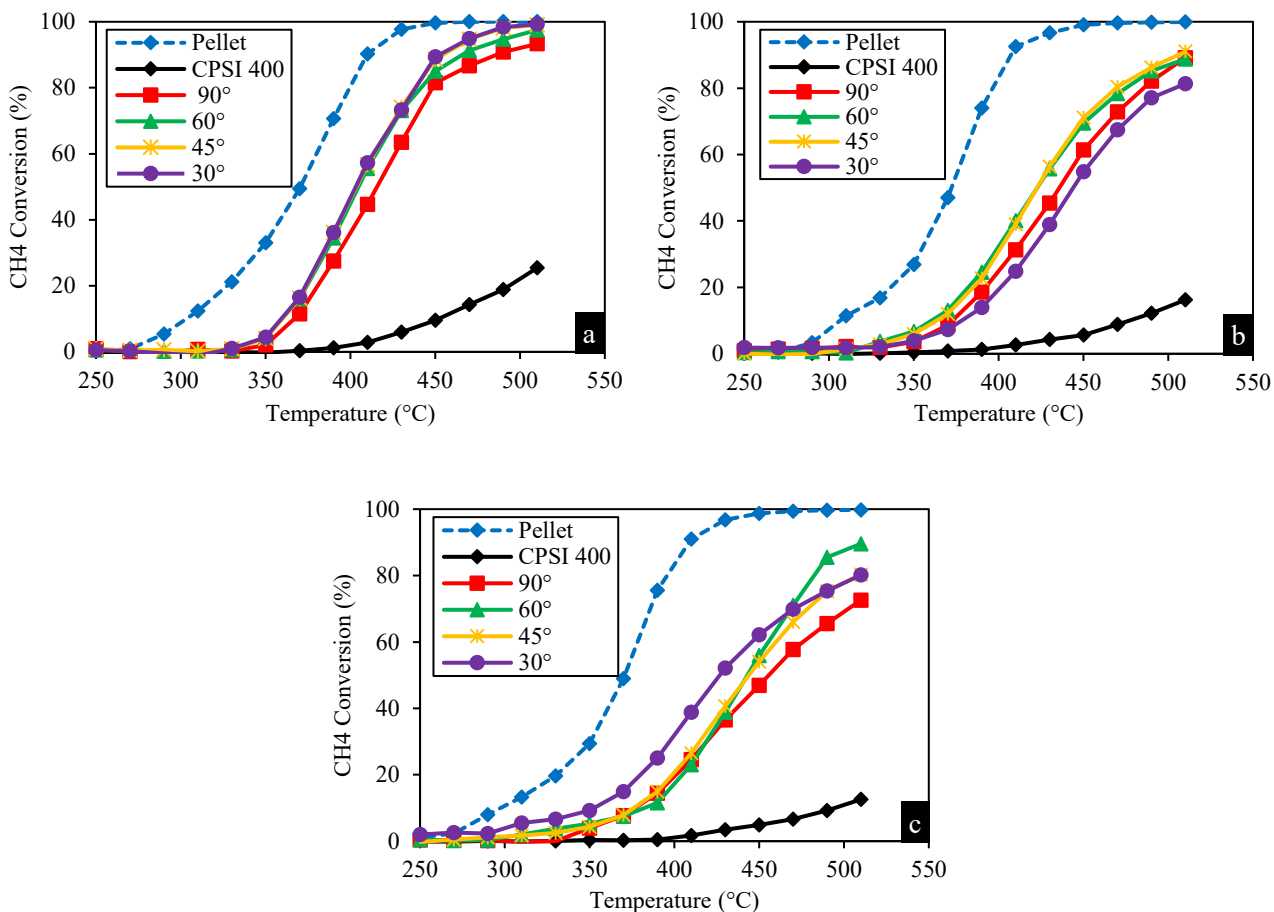
266

Figure 9. TEM images of catalyst washcoat, a) fresh catalyst (left); after 90 hours stability test (right).

267

268 3.3 Methane oxidation

269 Methane was practically unreactive from 200-250 °C, while the conversions increased continuously thereafter
270 from 250 °C. Figure 10a-c show that the pellets are catalytically active and that no significant change in activity
271 was observed at different GHSVs.



272

273

274 Figure 10 Effect of structure on methane conversion; a) GHSV 400 h⁻¹, b) GHSV 800 h⁻¹, c) GHSV 1200 h⁻¹ (CH₄: 5%, O₂: 10%, He:
275 85%).

276

277 All 3D printed substrates showed superior catalytic activity than the conventional CPSI 400 structure. For
278 instance, at 510 °C and GHSV of 1200 h⁻¹, methane conversion is 12.6% on the commercial structure, while
279 this value is 72.6% for the 90 ° structure, 80.1% for both 30 ° and 45 °, and 89.6% for the 60 °. Another
280 interesting observation is the effect of GHSV on performance of 3D printed substrates. At low GHSV (e.g. 400
281 h⁻¹), all 3D printed substrates have a very similar conversion at temperature range of 350-510 °C, however,
282 increasing the flow rate influenced their catalytic performance. For example, at GHSV of 1200 h⁻¹ the 30 °
283 structure shows better conversion at the temperature range of 300-450 °C, while the 60 ° structure shows the
284 highest conversion at temperatures above 450 °C. At high velocities, the 90 ° structure, which is the most similar
285 in structure to the conventional substrate, shows the lowest activity compared to the other 3D printed structures.
286 In general, these results clearly show that increasing complexity of the channel structure in the 3D printed
287 substrates increases catalytic activity by altering the flow regime and enhancing the mass transfer/turbulence.

288 Incidentally, the catalyst activity was lower when washcoated on the substrates, relative to pellets, due to the
289 void volume and heat transfer into the substrate, which lowered the overall catalyst temperature.

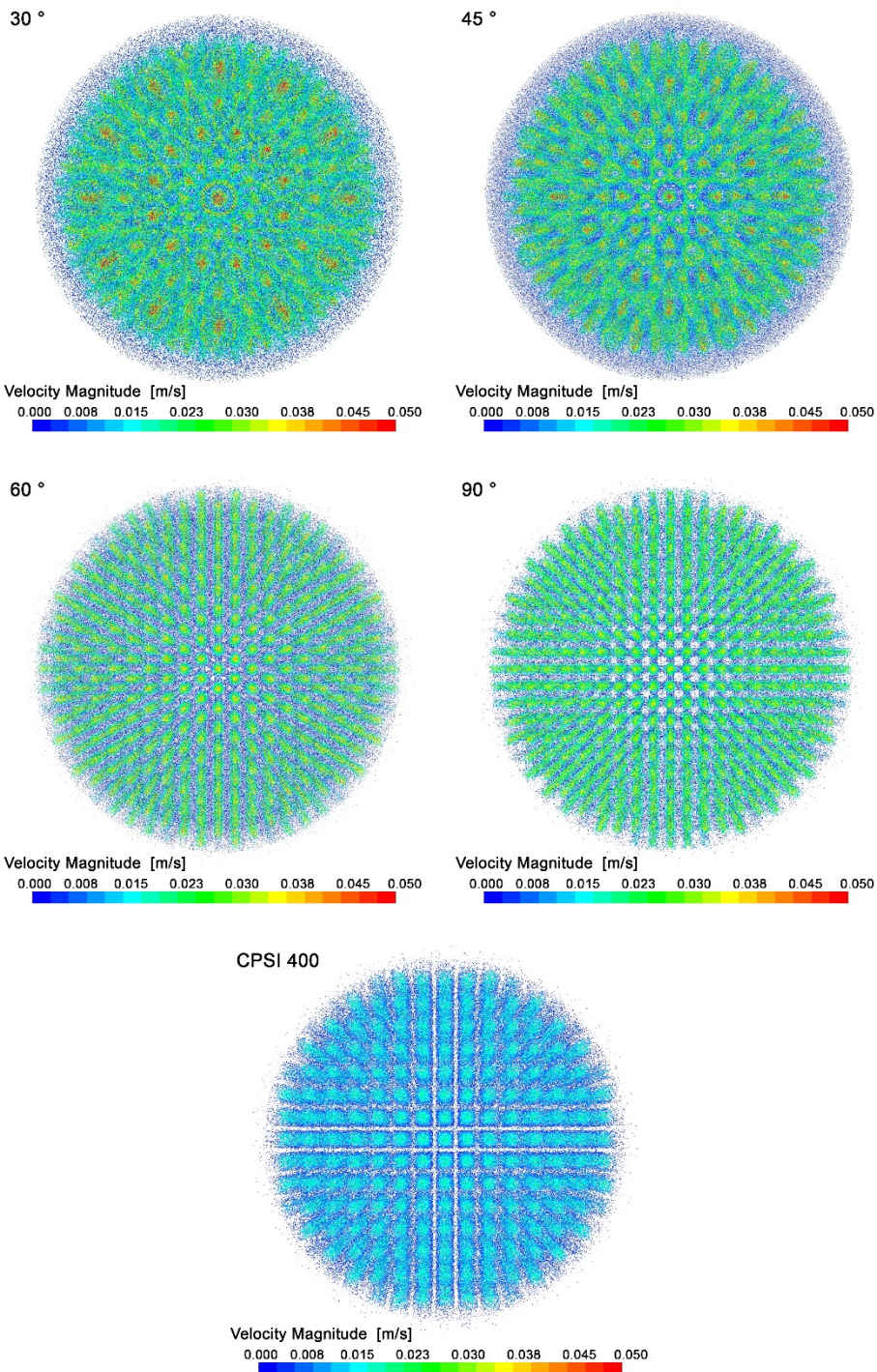
290 The increased catalytic activity is also rationalised by the higher surface areas in the 3D printed substrates (Table
291 4), which result from the unique arrangement of 3-dimensionally oriented layers, thereby exposing a higher
292 proportion of substrate to the external surface. To keep the experimental conditions same, the amount of catalyst
293 loading on the substrate kept similar (e.g. around 0.1 mg).

294 The preparation of a substrate with lower wall thickness and higher CPSI using more advanced 3D printing
295 technology, e.g. SLA or DLP, will improve the catalytic performance; such trials are currently under
296 investigation by the authors.

297 Table 4. Relation between structure and physical properties of the substrates (wall thickness of 3D printed substrate =
298 0.59 mm, wall thickness of commercial substrate = 0.18 mm).

Structure	Surface Area (m ² .L ⁻¹)	Weight of washcoat (mg)	Weight of substrate (mg)
30 °	3.628	0.104	8.538
45 °	3.633	0.103	8.407
60 °	3.630	0.104	8.286
90 °	3.629	0.095	7.755
CPSI 400	2.876	0.097	2.285

299
300 Figure 11 compares the velocity magnitude vectors for both conventional and 3D printed structures. Generally,
301 the 3D printed structure benefits from a higher velocity magnitude and therefore higher turbulence inside the
302 channels. The dark blue colour represents low velocity vectors, which mostly occurs near the walls, while orange
303 and red colours represent high velocity vectors which occurs in the centre of the channels. These regions (orange
304 and red colours) do not exist for commercial substrates and are in the order 30 ° > 45 ° > 60 ° > 90 ° for the 3D
305 printed substrates. Therefore, we tentatively assign the higher conversion of methane over the 30 ° substrate in
306 the temperature range of 300-450 °C to its higher turbulence at this GHSV. It should be noted that the 60 and
307 90 ° exhibit a lower degree of irregularity compared to 30 ° and 45 °.



308

309

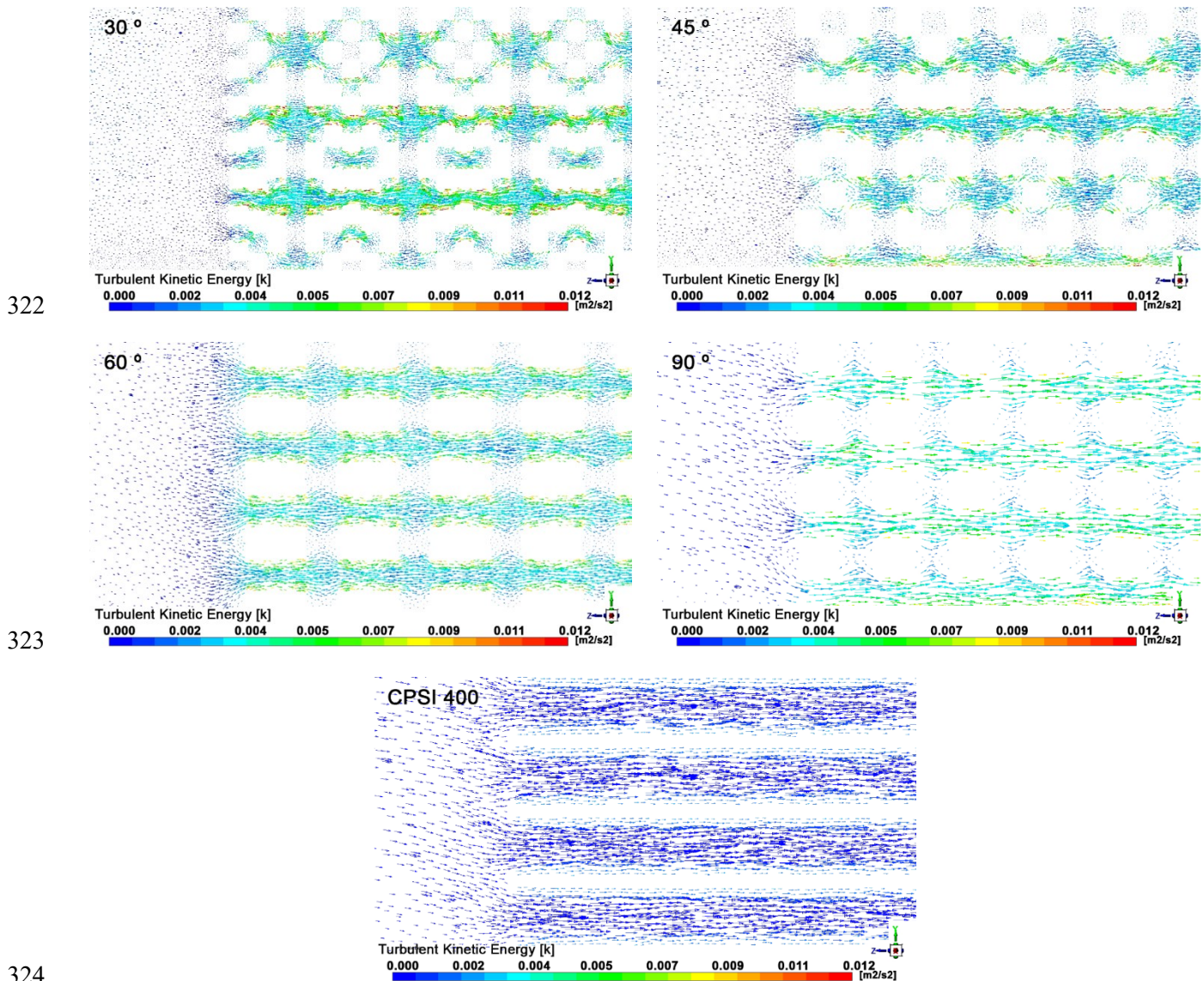
310

311 Figure 11. Frontal view of velocity magnitude vectors in the fluid domain for different substrate structures (Fluid: air at 25 °C; GHSV:
 312 1200 h⁻¹).

313 Turbulent kinetic energy is used to represent the intensity of turbulence in a given region. Figure 12 illustrates
 314 the turbulent kinetic energy vector inside the channels across the flow direction. While this value is relatively
 315 small (blue colour) and mainly in one direction for the conventional structure, higher turbulent kinetic energy
 316 and in different directions is observed for the 3D printed structures. Orange and red vectors are close to the
 317 walls, especially where the walls intersect. This is due to the rotation of the wall across the z-axis which leads
 318 to the formation of a complex structure. It also can be concluded that the magnitude of turbulent kinetic energy

319 is less for more regular structures (e.g. 60° or 90°). The distribution of turbulent kinetic energy is also more
320 uniform for such structures.

321



324

325

326

327 Static pressure profile across the z-axis of substrates is shown in Figure 13. The maximum change in static
328 pressure is observed for the more complex structures, particularly the 30° and 45° , which provide the most
329 turbulence. Pressure drops over 60° and 90° structures are milder compared to the 30° and 45° structures but
330 still more than that for the straight-channelled conventional structures.

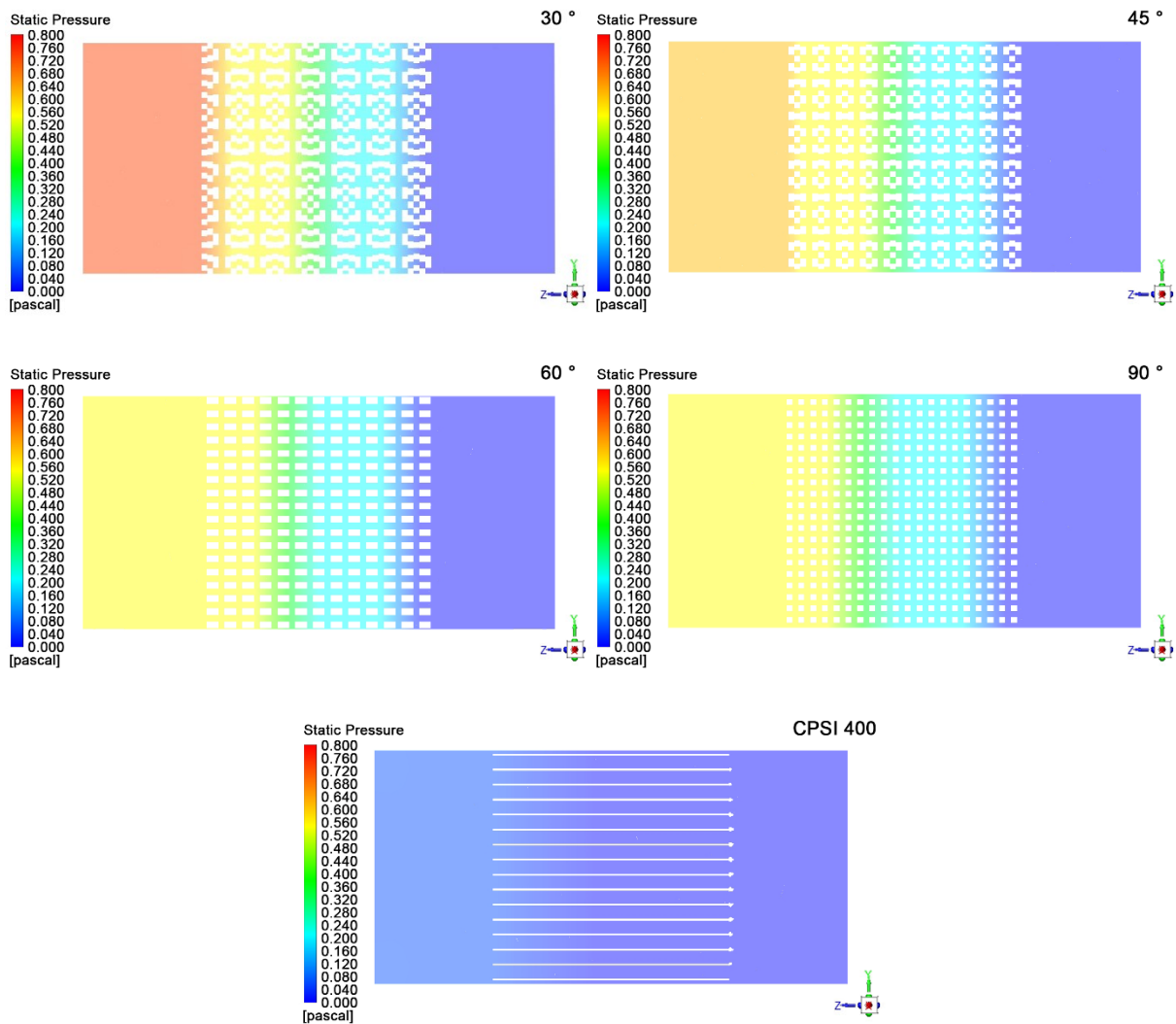


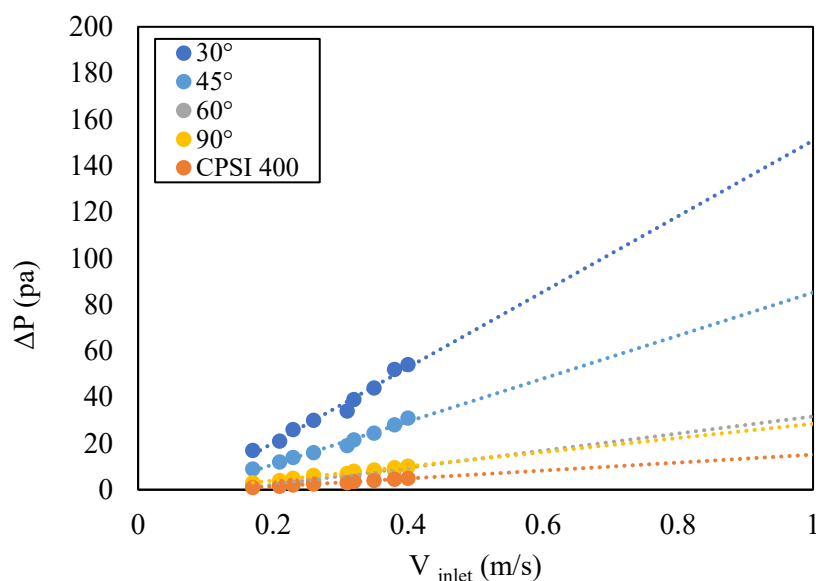
Figure 13 Static pressure profile across the substrate with different structures (GHSV=1200 h⁻¹).

3.4 Backpressure measurement

An experimental method was used to measure the backpressure over different structures at different air inlet velocities. Figure 14 compares the backpressure over different substrate structures for the inlet velocity up to 1.0 m.s⁻¹. As expected, the 3D printed structures show higher backpressure compared to the conventional substrates with straight channels. This is due to induced turbulence in these structures, which causes irregular fluctuations and mixing, in contrast to the laminar flow regime with higher velocity inside the straight channels. The backpressure is much less for the structures with more regularity (e.g. 60 ° and 90 °). This is in line with the CFD analysis results where the 30 ° and 45 ° structures exhibited more turbulence.

The highest contribution to backpressure in a real diesel engines is from the diesel particulate filter (DPF) in the after treatment system. The maximum recommended exhaust backpressure by VERT (Verification of Emission Reduction Technologies) for DPF varies. The values are 40 kPa for engines with less than 50 kW power, 20

347 kPa for 50-500 kW engines and 10 kPa for engines with power more than 500 kW[48]. The results in Figure 14
348 suggest that backpressure for the 60 ° and 90 ° are close to that for the commercial substrate, which makes these
349 structures suitable for commercial applications.



350
351 Figure 14 Effect of inlet gas velocity on backpressure over different structures.

352 353 4. Conclusions

354 Catalytic converter substrates prepared by 3D printing of cordierite showed improved catalytic activity in
355 methane oxidation relative to a conventional commercial honeycomb structure. It was shown that the substrates
356 with irregular structures had higher conversion due to the higher turbulent kinetic energy in these structures.
357 The findings provide proof of concept evidence that 3D printing is a suitable means of designing a catalytic
358 converter prototype with higher reaction activity than currently available. The findings have implications for
359 the design and potential mass production of new catalytic materials.

360 361 Acknowledgements

362 This research is funded by an Innovate UK Knowledge Transfer Partnerships (KTP) number 10723 and G-
363 volution Ltd.

364 References

- 365 [1] Reşitoğlu İA, Altinişik K, Keskin A. The pollutant emissions from diesel-engine vehicles and
366 exhaust aftertreatment systems. *Clean Technologies and Environmental Policy* 2015;17(1):15-
367 27.
368 [2] Lloyd AC, Cackette TA. Diesel Engines: Environmental Impact and Control. *Journal of the*
369 *Air & Waste Management Association* 2001;51(6):809-47.

- 370 [3] IARC. DIESEL ENGINE EXHAUST CARCINOGENIC. France: International Agency for
371 Research on Cancer, World Health Organisation; 2012.
- 372 [4] Cheenkachorn K, Poompipatpong C, Ho CG. Performance and emissions of a heavy-duty
373 diesel engine fuelled with diesel and LNG (liquid natural gas). *Energy* 2013;53:52-7.
- 374 [5] Saleh HE. Effect of variation in LPG composition on emissions and performance in a dual fuel
375 diesel engine. *Fuel* 2008;87(13-14):3031-9.
- 376 [6] Liu J, Yang F, Wang H, Ouyang M, Hao S. Effects of pilot fuel quantity on the emissions
377 characteristics of a CNG/diesel dual fuel engine with optimized pilot injection timing. *Applied*
378 *Energy* 2013;110:201-6.
- 379 [7] Nathan SS, Mallikarjuna JM, Ramesh A. An experimental study of the biogas-diesel HCCI
380 mode of engine operation. *Energy Conversion and Management* 2010;51(7):1347-53.
- 381 [8] Wei LJ, Yao CD, Wang QG, Pan W, Han GP. Combustion and emission characteristics of a
382 turbocharged diesel engine using high premixed ratio of methanol and diesel fuel. *Fuel*
383 2015;140:156-63.
- 384 [9] Saravanan N, Nagarajan G, Sanjay G, Dhanasekaran C, Kalaiselvan KM. Combustion analysis
385 on a DI diesel engine with hydrogen in dual fuel mode. *Fuel* 2008;87(17-18):3591-9.
- 386 [10] Reiter AJ, Kong SC. Combustion and emissions characteristics of compression-ignition engine
387 using dual ammonia-diesel fuel. *Fuel* 2011;90(1):87-97.
- 388 [11] Wei L, Geng P. A review on natural gas/diesel dual fuel combustion, emissions and
389 performance. *Fuel Processing Technology* 2016;142:264-78.
- 390 [12] Abdelaal MM, Hegab AH. Combustion and emission characteristics of a natural gas-fueled
391 diesel engine with EGR. *Energy Conversion and Management* 2012;64:301-12.
- 392 [13] Korakianitis T, Namasivayam AM, Crookes RJ. Natural-gas fueled spark-ignition (SI) and
393 compression-ignition (CI) engine performance and emissions. *Progress in Energy and*
394 *Combustion Science* 2011;37(1):89-112.
- 395 [14] Ashok B, Denis Ashok S, Ramesh Kumar C. LPG diesel dual fuel engine – A critical review.
396 *Alexandria Engineering Journal* 2015;54(2):105-26.
- 397 [15] Avila P, Montes M, Miró EE. Monolithic reactors for environmental applications: A review on
398 preparation technologies. *Chem Eng J* 2005;109(1):11-36.
- 399 [16] Heck RM, Farrauto RJ. Automobile exhaust catalysts. *Applied Catalysis A: General*
400 2001;221(1):443-57.
- 401 [17] Williams JL. Monolith structures, materials, properties and uses. *Catalysis Today* 2001;69(1-
402 4):3-9.
- 403 [18] Carty WM, Lednor PW. Monolithic ceramics and heterogeneous catalysts: honeycombs and
404 foams. *Current Opinion in Solid State and Materials Science* 1996;1(1):88-95.
- 405 [19] Liu PS, Chen GF. Chapter Five - Fabricating Porous Ceramics. In: Liu PS, Chen GF, editors.
406 *Porous Materials*. Boston: Butterworth-Heinemann; 2014, p. 221-302.
- 407 [20] Manfe MM, Kulkarni K, Kulkarni A. Industrial application of monolith catalysts/reactors. *Int*
408 *J Adv Eng Res Stud*(E-ISSN2249–8974) 2011.
- 409 [21] Wiehl J, Vogt CD. Ceramic ultra-thin-wall substrates for modern catalysts. *MTZ worldwide*
410 2003;64(2):8-11.
- 411 [22] Kašpar J, Fornasiero P, Hickey N. Automotive catalytic converters: current status and some
412 perspectives. *Catalysis Today* 2003;77(4):419-49.
- 413 [23] Müller-Haas K, Rice M. Innovative metallic substrates for exhaust emission challenges for
414 gasoline and diesel engines. *SAE Technical Paper*; 2005.
- 415 [24] Santos H, Costa M. Evaluation of the conversion efficiency of ceramic and metallic three way
416 catalytic converters. *Energy Conversion and Management* 2008;49(2):291-300.
- 417 [25] Bunimovich GA, Strots VO, Matros YS, Mirosh EA. Reversed Flow Converter: Fundamentals
418 of the Design. *SAE International*; 1999.
- 419 [26] Strots VO, Bunimovich GA, Matros YS, Zheng M, Mirosh EA. Novel Catalytic Converter for
420 Natural Gas Powered Diesel Engines. *SAE International*; 1998.
- 421 [27] Liu B, Checkel MD, Hayes RE. Experimental study of a reverse flow catalytic converter for a
422 dual fuel engine. *Canadian Journal of Chemical Engineering* 2001;79(4):491-506.

- 423 [28] Matros YS, Bunimovich GA, Strots VO, Mirosh EA. Reversed flow converter for emission
424 control after automotive engines. *Chemical Engineering Science* 1999;54(13):2889-98.
- 425 [29] Bella G, Rocco V, Maggiore M. A Study of Inlet Flow Distortion Effects on Automotive
426 Catalytic Converters. *Journal of Engineering for Gas Turbines and Power* 1991;113(3):419-26.
- 427 [30] Karvounis E, Assanis DN. The effect of inlet flow distribution on catalytic conversion
428 efficiency. *International journal of heat and mass transfer* 1993;36(6):1495-504.
- 429 [31] Agrawal T, Banerjee VK, Sikarwar BS, Bhandwal M. Optimizing the Performance of Catalytic
430 Converter Using Turbulence Devices in the Exhaust System. Singapore: Springer Singapore;
431 2019:333-42.
- 432 [32] Brück R, Pace L, Presti M. Turbulent Flow Catalyst: Solution for Euro 5 and beyond. Oct;
433 2006.
- 434 [33] Emitec. Radially open structures (PE-Design®); 2019. Available from:
435 <https://www.emitec.com/en/technology/catalyst-substrates/structured-foils/>. [Accessed
436 November 2019].
- 437 [34] Faes M, Valkenaers H, Vogeler F, Vleugels J, Ferraris E. Extrusion-based 3D Printing of
438 Ceramic Components. *Procedia CIRP* 2015;28(Supplement C):76-81.
- 439 [35] Parra-Cabrera C, Achille C, Kuhn S, Ameloot R. 3D printing in chemical engineering and
440 catalytic technology: structured catalysts, mixers and reactors. *Chemical Society Reviews*
441 2018;47(1):209-30.
- 442 [36] Chen Z, Li Z, Li J, Liu C, Lao C, Fu Y, et al. 3D printing of ceramics: A review. *Journal of the*
443 *European Ceramic Society* 2019;39(4):661-87.
- 444 [37] Goren R, Gocmez H, Ozgur C. Synthesis of cordierite powder from talc, diatomite and alumina.
445 *Ceramics International* 2006;32(4):407-9.
- 446 [38] Gonzalez-Velasco J, Gutierrez-Ortiz M, Ferret R, Aranzabal A, Botas J. Synthesis of cordierite
447 monolithic honeycomb by solid state reaction of precursor oxides. *Journal of materials Science*
448 1999;34(9).
- 449 [39] Doyle AM, Postolache R, Shaw D, Rathon R, Tosheva L. Methane oxidation over zeolite
450 catalysts prepared from geothermal fluids. *Microporous and Mesoporous Materials*
451 2019;285:56-60.
- 452 [40] Petrov AW, Ferri D, Kröcher O, van Bokhoven JA. Design of Stable Palladium-Based Zeolite
453 Catalysts for Complete Methane Oxidation by Postsynthesis Zeolite Modification. *ACS*
454 *Catalysis* 2019;9(3):2303-12.
- 455 [41] Bianchi CL, Pirola C, Ragaini V. Choosing the best diluent for a fixed catalytic bed: The case
456 of CO hydrogenation. *Catalysis Communications* 2006;7(9):669-72.
- 457 [42] ANSYS FLUENT User's Guide 12.0. *Using Flow Boundary Conditions*. 2009.
- 458 [43] Stuecker JN, Witze PO, Ferrizz RM, Cesarano III J, Miller JE. Revolutionary systems for
459 catalytic combustion and diesel catalytic particulate traps. Sandia National Laboratories; 2004.
- 460 [44] San Marchi C, Kouzeli M, Rao R, Lewis JA, Dunand DC. Alumina–aluminum
461 interpenetrating-phase composites with three-dimensional periodic architecture. *Scripta*
462 *Materialia* 2003;49(9):861-6.
- 463 [45] Mamatha S, Biswas P, Das D, Johnson R. 3D printing of cordierite honeycomb structures and
464 evaluation of compressive strength under quasi-static condition. *International Journal of*
465 *Applied Ceramic Technology* 2020;17(1):211-6.
- 466 [46] Chen Z, Liu C, Li J, Zhu J, Liu Y, Lao C, et al. Mechanical properties and microstructures of
467 3D printed bulk cordierite parts. *Ceramics International* 2019;45(15):19257-67.
- 468 [47] Thommes M. Physical Adsorption Characterization of Nanoporous Materials. *Chemie*
469 *Ingenieur Technik* 2010;82(7):1059-73.
- 470 [48] Mayer A. Number-based emission limits, VERT-DPF-verification procedure and experience
471 with 8000 retrofits. VERT, Switzerland 2004.
- 472